ROYAL SOCIETY
OF CHEMISTRY

EDGE ARTICLE

Check for updates

Decimeter-length elastic organic crystals capable of mechanical post-processing and optical waveguide modulation at 77 K†

Tingting Ji, Xuesong Yang, Quanliang Chen and Hongyu Zhang ⓘ *

The development of decimeter-length organic crystals that remain elastic, functional, and machinable at extremely low temperatures, such as in liquid nitrogen (LN) environments, is a great challenge. Here, we report two novel elastic organic crystals, **1** and **2**, derived from mono-benzene compounds. Crystals **1** are elastically bendable with decimeter-scale length (>10 cm) and exhibit better elastic bending ability at LN temperature compared to room temperature. In contrast, centimeter-length crystals **2** show reduced elasticity at LN temperature. Notably, crystals **1** can be cut and stripped at LN temperature. To the best of our knowledge, this is the first report on the cryogenic machinability of organic crystals. By crystallographic analyses of **1** and **2**, intermolecular interactions are shown to be responsible for their distinct crystal habits and cryogenic machinability. In addition, after stripping, crystals **1** exhibit programmable optical waveguide properties that vary in proportion to the crystal width and thus have the potential for applications as tunable wavelength modulators, capable of real-time two-dimensional motion detection in cryogenic environments. This material not only advances the field of flexible organic crystals but also opens up new possibilities for the development of smart materials that can be used under extreme conditions.

Introduction

Mechanically bendable organic crystals, a newly emerged class of engineered and functional materials, typically have narrow shapes with lengths ranging from micrometers to centimeters.[1–5] The unique properties of these materials, including but not limited to anisotropy, regular packing order, light weight, intense emission, and high carrier mobility, make them advantageous for the development of wearable devices,[6–8] flexible optoelectronics,[9–11] biocompatible sensors,[12,13] and actuators.[14–16] Additionally, mechanical flexibility gives some centimeter- and micrometer-size crystals processability and maneuverability under ambient conditions. For example, the high-precision mechanical manipulation technique to construct crystalline organic photonic integrated circuits and the straightforward top-down approach involving cutting centimeter-scale elastic organic crystals into fibers have been recently developed by Chandrasekar[17] and Hayashi,[18] respectively. Through optimizing supramolecular structures, several ultralow-temperature elastic organic crystals that can be bent

even in liquid nitrogen (LN, 77 K) have been reported recently.[19–22] However, it is still a critical challenge in this field to develop decimeter-length organic crystalline materials that remain flexible, functional, and machinable at LN temperature. Most organic materials, including plastics and elastomers,[23–25] tend to become brittle and challenging to process at 77 K, limiting their utility in extreme environments, such as those encountered in space exploration and polar research. This limitation is particularly critical when flexibility and mechanical manipulability are essential for their intended applications. In addition, the precise control and modulation of optical signals under extreme conditions are vital for advancing optical communications and sensing technologies.[26–29] Optical signal transmission and modulation in low-temperature environments face unique challenges, such as the effects of thermal shrinkage of materials[30] and temperature dependence of optical properties.[31] Therefore, there is an urgent need to develop innovative materials that can demonstrate low-temperature flexibility, processability, and tunable optical properties.

Mono-benzene π-systems, one of the smallest aromatic units, have been widely used to develop a variety of highly efficient solid emitters.[32–37] For example, Xiang *et al.* reported that terephthalonitrile-based mono-benzene structures with an electronic push–pull system have strong solid-state fluorescence.[32] Substituent modifications on mono-benzene structures can effectively regulate fluorescence properties ranging from blue to red and intermolecular interactions, demonstrating

great advantages in developing flexible organic crystals with the unique optical functions of optical waveguides,[38] polarization materials,[39] and lasers.[40] In this work, we designed two novel flexible organic crystals **1** and **2** with strong blue emission by replacing one fluorine atom of the mono-benzene compound 2,3,5,6-tetrafluoroterephthalonitrile with 2-(2-aminoethoxy)-1-ethanol and propanolamine, respectively. While bearing the same mono-benzene building block, crystals **1** and **2**, with narrow shapes, display quite different growth lengths, LN-temperature elasticity, and LN-temperature manipulability. By carefully investigating the crystal structures, we demonstrated that the well-designed intermolecular interactions in crystal **1** were responsible for the enhanced one-dimensional growth capability, and excellent LN-temperature elasticity and machinability. The decimeter-scale crystal **1**, after processing, showed width-dependent waveguide output modulation ability. The magnitude of the waveguide modulation decreased as the crystal width decreased, which enabled precise adjustment of the optical outputs through simple dimensional changes. The potential of crystals **1** as optical wavelength modulators and a novel spectral sensing system capable of real-time, two-dimensional motion detection in cryogenic environments has been demonstrated by combining these unique properties.

Results and discussion

Two mono-benzene compounds **1** and **2** with different side chains were synthesized in high isolated yields by a simple one-step reaction between 2-(2-aminoethoxy)-1-ethanol (Fig. 1a and S1†) or propanolamine (Fig. 1d and S2†) and 2,3,5,6-

tetrafluoroterephthalonitrile followed by column chromatography purification. Pale green narrow crystals **1** and **2** with mechanical elasticity and intense blue emissions were obtained by solution diffusion methods (Fig. 1b–h). The diffusion of cyclohexane into a dichloromethane solution of **1** produced decimeter-level, high-quality crystals, which far exceeded the lengths of previously reported elastic organic crystals. Despite the large size of the crystals, they retain excellent mechanical properties. As shown in Fig. 1c, a 10.25 cm crystal **1** (Fig. S6†) can be bent using both hands. By a similar solution diffusion process, centimeter-sized crystals **2** were obtained (Fig. 1e). The absorption and emission spectra of crystals **1** and **2** are shown in Fig. 1f. Upon excitation with 375 nm ultraviolet light, crystals **1** and **2** exhibited maximum emission peaks at 466 nm and 467 nm at 298 K, respectively. Additionally, the absolute fluorescence quantum yields of crystals **1** and **2** were measured to be 0.44 and 0.32 (Fig. S7†), respectively. Crystals **1** and **2** exhibited excellent elasticity and could be bent repeatedly when external forces are applied under ambient conditions (Fig. 1g and h). When subjected to external forces in LN, crystal **2**, unlike crystal **1**, was prone to fracture (Fig. S8†). To quantitatively evaluate the mechanical bendability of the crystals, the maximum expansion/contraction ratio (maximum elastic strain, ε) of the inner/outer arcs of the bent crystals without cracking was determined using a reported method.[41,42] The method involved winding crystals of different thicknesses around a cylinder to form a semicircle (Fig. 1i and j). As shown in Fig. 1k, 15 samples of crystals **1** with different thicknesses were selected. To reduce error, each crystal was cut into two sections and wound on a capillary tube with an outer diameter of 0.52 mm for the
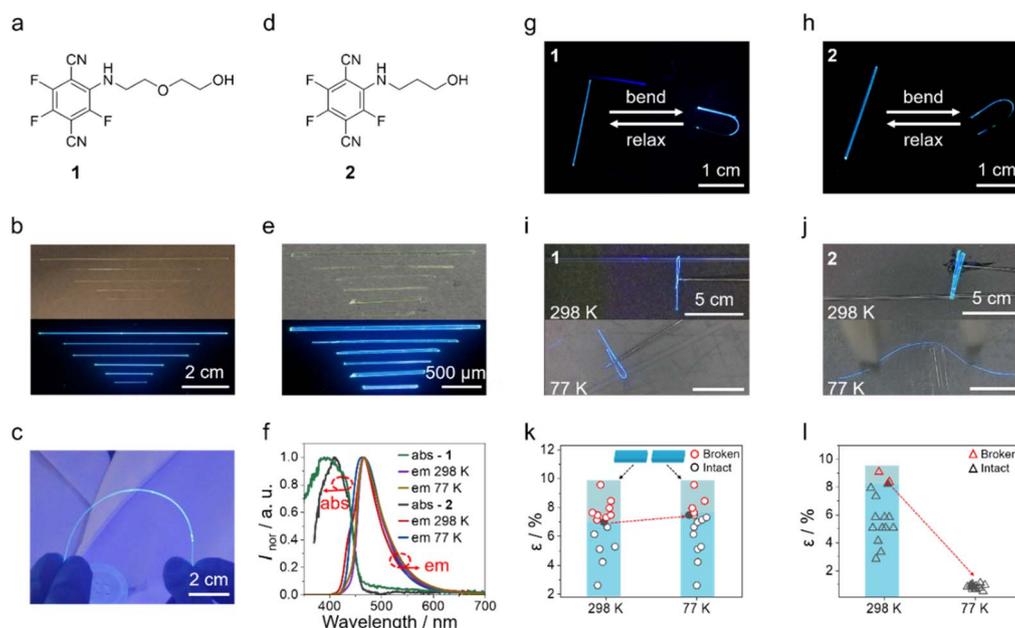
Fig. 1 (a) Chemical structure of crystal **1**. (b) Photographs of crystal **1** under daylight and ultraviolet light. (c) Photograph of a decimeter-level crystal **1** bent by hands. (d) Chemical structure of crystal **2**. (e) Photographs of crystal **2** under daylight and ultraviolet light. (f) Absorption and emission spectra of crystals **1** and **2**. (g and h) Photographs of crystals **1** (g) and **2** (h) repeatedly bent at 298 K. (i and j) Photographs of the greatest level that could be formed before crystals **1** (i) and **2** (j) were broken at 298 K and 77 K; the capillary has diameters of 0.52 mm (i) and 0.58 mm (j). (k and l) Fifteen sets of parallel experiments were conducted to determine the maximum elastic strain of crystals **1** (k) and **2** (l) at 298 K and 77 K.

experiment at room temperature and LN temperature. The calculated maximum ε for crystal **1** was 6.98% at room temperature and 7.47% at LN temperature (thickness: 0.039 mm at 298 K, 0.042 mm at 77 K). Similarly, crystals **2** exhibited excellent elasticity at room temperature (thickness = 0.052 mm, ε = 8.23%). However, the bending capacity of crystals **2** was significantly decreased at 77 K (ε = 0.83%) (Fig. 1l and Table S1†).

To investigate the reasons for the different mechanical properties at room and low temperatures and distinct crystal habits of crystals **1** and **2** (Fig. 1), single-crystal X-ray diffraction (XRD) experiments were performed on crystals **1** and **2** at 298 and 100 K (Fig. 2). As shown in Fig. S9† the face index confirms that crystals **1** and **2** grow along the *a*-axis and *b*-axis and the bendable crystal planes are (010) and (100) (Fig. 2a–h), respectively. When crystal **1** was frozen by blowing in LN gas, the *a*, *b*, and *c*-axes shortened by −0.8%, −0.9%, and −1.6%, respectively (Fig. 2a and b), and the torsion angle between the benzene ring and side chain slightly decreased by 0.27°. The isotropic contraction of the crystal axis, combined with small conformation change, evidently resulted in more compact and stable crystals upon freezing.[20] Compared to crystal **1**, crystal **2** exhibited an anisotropic response to freezing, with the *a*- and *c*-axes contracted by −1.2% and −4.7%, respectively, while the *b*-axis expanded by 3.4% (Fig. 2c and d). This anisotropic

contraction of the crystal cells and conformational distortion of the molecules inevitably added additional internal tensile stresses.[19] This is one of the reasons for the worsening in mechanical properties of crystal **2** at LN temperature. As shown in Fig. 2i and j, the spatial arrangement of the N, O, and F atoms of crystals **1** and **2** results in abundant hydrogen-bonding interactions. When the crystal was subjected to external stress, the distance between the outer arc molecules increased, while the inner arc molecules became more contracted (Fig. 2f and h). The intermolecular hydrogen bonds effectively dissipate the bending energy and prevent the molecules from sliding over long distances, which enables crystals **1** and **2** to maintain excellent elasticity at room temperature. Crystals **1** and **2** exhibited markedly different elastic bending capacities at low temperatures compared to room temperature. To elucidate the underlying reasons for these variations, we analyzed the hydrogen bonding energy changes in crystals **1** and **2** at different temperatures. The energy frameworks were constructed using Crystal Explorer[43] and the B3LYP hybrid functional with the 6-31G(d,p) basis set, where semiempirical dispersion was included by using the D2 version of Grimme's dispersion. As shown in Fig. S10,† at 100 K, the hydrogen bonds in crystal **1** became stronger, while those in crystal **2** became weaker. To further illustrate the variation in hydrogen bond energies, we calculated the energies of individual hydrogen
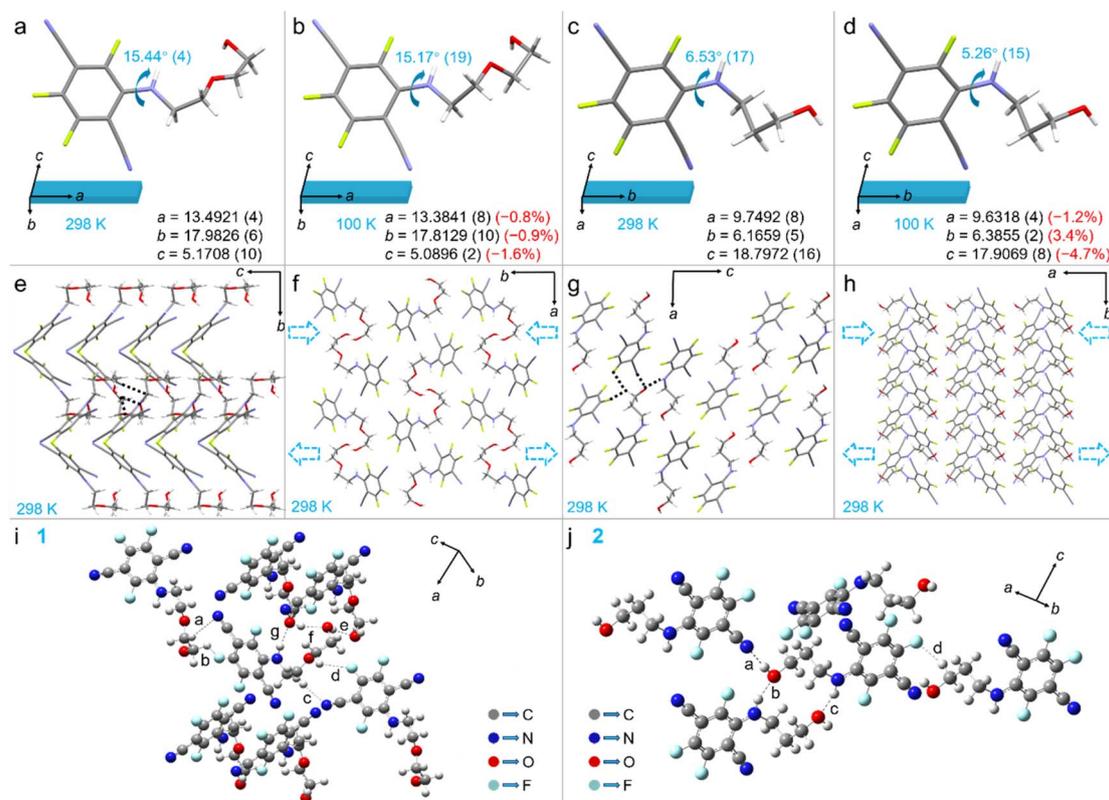

Fig. 2 (a–d) Molecular structures of crystal **1** (a and b) and **2** (c and d) determined at 298 K and 100 K. (e) Packing structure of crystal **1**: view down the (100) plane at 298 K. (f) Packing structure of crystal **1**: view down the (001) plane at 298 K and the expansion and contraction directions of the outer and inner arcs expected during bending. (g) Packing structure of crystal **2**: view down the (010) plane at 298 K. (h) Packing structure of crystal **2**: view down the (001) plane at 298 K, and the expansion and contraction directions of the outer and inner arcs expected during bending. (i and j) Types of hydrogen bonding for crystals **1** (i) and **2** (j).

bonds separately. Geometry optimizations of H atoms (with heavy atoms frozen) were conducted using the B3LYP-D3 (BJ)/6-311G(d) basis set with the Gaussian 09 package.[44] Frequency analysis was conducted to ensure there were no imaginary frequencies. Atoms-in-molecules (AIM) theory was used to analyze the properties of the position of the bond critical points (BCPs) of the hydrogen bonds to investigate the characteristics of the hydrogen bonds, based on which the energy of the hydrogen bonds was calculated.[45] As shown in Table S2,† the hydrogen bonding energies of crystal 1 at 100 K showed a generally increasing trend compared to at 298 K. For example, the energy of C–H···N increased from -0.515 kcal mol^{-1} to -1.740 kcal mol^{-1}, while that of C–H···F increased from -0.158 kcal mol^{-1} to -0.739 kcal mol^{-1}, and that of O–H···O increased from -3.744 kcal mol^{-1} to -4.658 kcal mol^{-1}. In contrast, when crystal 2 was frozen to 100 K, the hydrogen bonding energies decreased compared to 298 K. For example, C–H···N weakened from -4.692 kcal mol^{-1} to -2.146 kcal mol^{-1}, N–H···O weakened from -6.261 kcal mol^{-1} to -5.558 kcal mol^{-1}, and C–H···F weakened from -6.080 kcal mol^{-1} to -5.481 kcal mol^{-1} (Table S3†). The above results indicated that the difference in the variation of hydrogen bonding energies was the main reason for the different

mechanical properties of crystals 1 and 2 at low temperatures (77 K). Meanwhile, the structural differences between crystals 1 and 2 were also important factors influencing different growth patterns. As shown in Fig. 2e and g, compared to crystal 2, the introduction of an ether–oxygen bond in crystal 1 resulted in the formation of an O–H···O interaction. Additionally, the hydroxyl group at the end of the side chain formed additional hydrogen bonds with another molecule, including O–H···O, N–H···O, and C–H···N noncovalent bonds. The existence of ether–oxygen bonding significantly stabilized the crystal lattice. This might contribute to the formation of an extended structure along the (100) plane, which in turn promoted the growth of decimeter-level crystals 1.

Material machinability is a fundamental property determining a material's potential for various applications. The elastic and anisotropic sheet morphology of crystals 1 allowed them to be shaped into fibers, similar to splitting leaves, wood, or roots, by a post-processing method. As shown in Fig. 3a and b, crystal 1 was placed atop a silicon wafer and cut using a blade, which allowed it to be split into different lengths at room temperature. Tip splitting occurred when the crystals were cut, probably due to the anisotropic sheet form of the crystals, in which the weak interactions between the molecular layers were
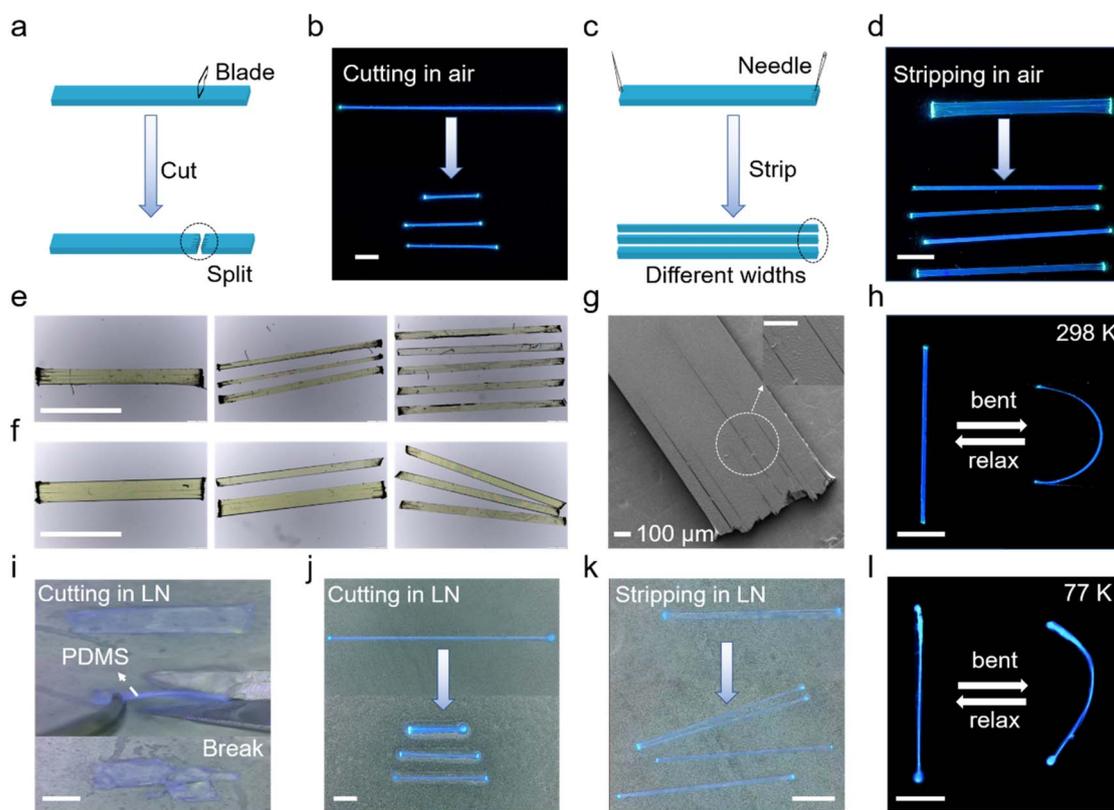

Fig. 3 (a) Schematic diagram of organic crystals cut to different lengths. (b) Photographs of crystal 1 cut to various lengths at room temperature. (c) Diagram of crystals 1 being stripped to different widths. (d) Photographs of crystals 1 stripped to various widths at room temperature. (e and f) Transmission micrographs of different thicknesses of crystals 1 stripped to different widths, 164 μm (e) and 219 μm (f). (g) Scanning electron microscope images of crystal 1 after machining. (h) Photographs of post-processed crystal 1 bent under external forces at room temperature. (i) Photographs of PDMS during machining. (j) Photographs of a crystal 1 cut to different lengths at LN temperature. (k) Photographs of a crystal 1 stripped to different widths at LN temperature. (l) Photographs of a post-processed crystal 1 bent under external forces at LN temperature. All scales are 2 mm unless stated otherwise.

broken (Fig. S11†). As shown in Fig. 3c and d, a crystal was machined to different widths by stripping it with the tip of a needle at the split (Movie S1†). To demonstrate that different thicknesses of crystals can be stripped, a crystal with a width of 404 μm and thickness of 164 μm was split to a minimum width of 80 μm (Fig. 3e). Similarly, another crystal with a thickness of 219 μm was manipulated to generate different widths (Fig. 3f). As shown in Fig. 3g, the processed crystal was observed using a scanning electron microscope to have a flat surface without breakage and could still be bent repeatedly (Fig. 3h). Most organic materials, such as polymers, are rigid, brittle, and difficult to machine at ultra-low temperatures.[3,38,46–49] For example, when a polydimethylsiloxane (PDMS) film was placed in liquid nitrogen and machined with scissors, it underwent a brittle fracture under external forces (Fig. 3i and Movie S2†). In contrast, crystal 1 in LN was still easily machined and could

be cut and stripped into thinner crystals (Fig. 3j, k and Movie S3†), maintaining excellent elasticity at LN temperature (Fig. 3l). The above experiments demonstrated the machinability of crystals 1 at both room and LN temperatures.

Flexible organic crystals have been recognized for their great potential in optical transmission within the visible spectrum and near-infrared region.[50–52] To ascertain the optical waveguide characteristics of the machined crystals, optical loss coefficients (OLCs) were evaluated for different widths of crystal 1. As shown in Fig. 4a–d, crystals 1 of the same length and thickness but with different widths (0.372 mm, 0.300 mm, 0.228 mm, 0.072 mm) were tested for optical waveguide characteristics. Distance-dependent emission spectra were obtained by uniformly irradiating the crystals from different positions using a 355 nm laser and capturing the emission spectra at the ends of the crystals (Fig. 4e). The emission intensity decreased with
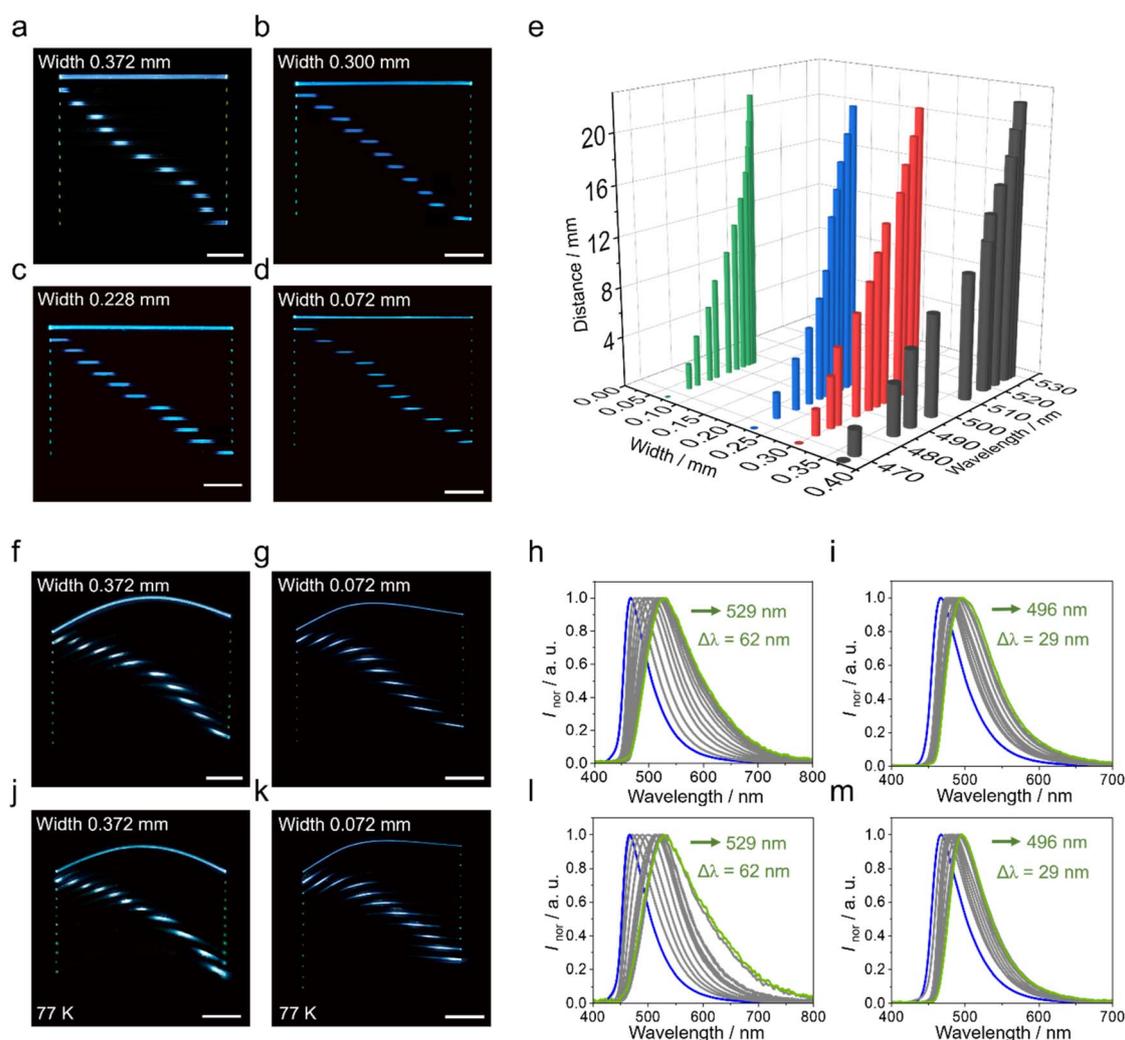
Fig. 4 (a–d) Images of crystals 1 with different widths used as waveguides: 0.372 mm (a), 0.300 mm (b), 0.228 mm (c) and 0.072 mm (d). (e) Plot of crystal widths, emission peak position and excitation position *versus* distance from the collected optical signal. (f and g) Images of crystals 1 with different widths used as waveguides in the bent state: 0.372 mm (f) and 0.072 mm (g). (h and i) Normalized fluorescence spectra for acquisitions at different excitation positions. Panels (h) and (i) correspond to the crystals shown in panels (f) and (g), respectively. (j and k) Images of crystals 1 with different widths used as waveguides in the bent state at 77 K: 0.372 mm (j) and 0.072 mm (k). (l and m) Normalized fluorescence spectra for acquisitions at different excitation positions. Panels (l) and (m) correspond to the crystals shown in panels (j) and (k), respectively. All the scales in the diagrams are 5 mm.

increasing distance from the irradiation point, which was attributed to optical loss (Fig. S12†). After fitting the collected data using the reported method,[53,54] the OLC of the emission peak was calculated to be 0.199 dB mm^{-1} for the 0.372 mm width, 0.161 dB mm^{-1} for the 0.300 mm width, 0.123 dB mm^{-1} for the 0.228 mm width, and 0.106 dB mm^{-1} for the 0.072 mm width of crystal **1** (Fig. S13†). The emission spectrum was gradually red shifted with increasing distance from the irradiation point to the signal acquisition location, with a maximum redshift wavelength of 62 nm, which was attributed to the self-absorption of crystal **1** (Fig. 1f and S14†). As shown in Fig. S13,† the optical loss of the crystals gradually decreased with decreasing width, suggesting that narrow crystals had lower probability of defects.[55] As a result, the self-absorption effect was weakened, resulting in a reduced redshift of the wavelength. Correspondingly, self-absorption also decreased, resulting in a reduced redshift of the wavelength. The

relationship between the crystal width and wavelength change was presented as an exponential relationship (Fig. S15†). In Fig. 4f and g, optical loss experiments were conducted on crystals **1** of different widths (0.372 mm, 0.072 mm) in the bent state. The OLCs of the maximum emission peak were calculated to be 0.208 dB mm^{-1} for the 0.372 mm width, and 0.200 dB mm^{-1} for the 0.072 mm width of crystals **1** in the bent state (Fig. S16†). The wavelength variations of different widths in the bent state were consistent with those in the straight state (Fig. 4h and i). As shown in Fig. 2a and b, crystals **1** were conformationally stable at room and LN temperatures, allowing stable luminescence properties. In Fig. 4j and k, crystals of various widths maintained optical signal transmission at 77 K, with the wavelength redshift increasing as the width increased (Fig. 4l and m). The OLC was 0.282 dB mm^{-1} for the 0.372 mm width, and 0.205 dB mm^{-1} for the 0.072 mm width of crystal **1** at 77 K (Fig. S17†). The above experiments demonstrated the
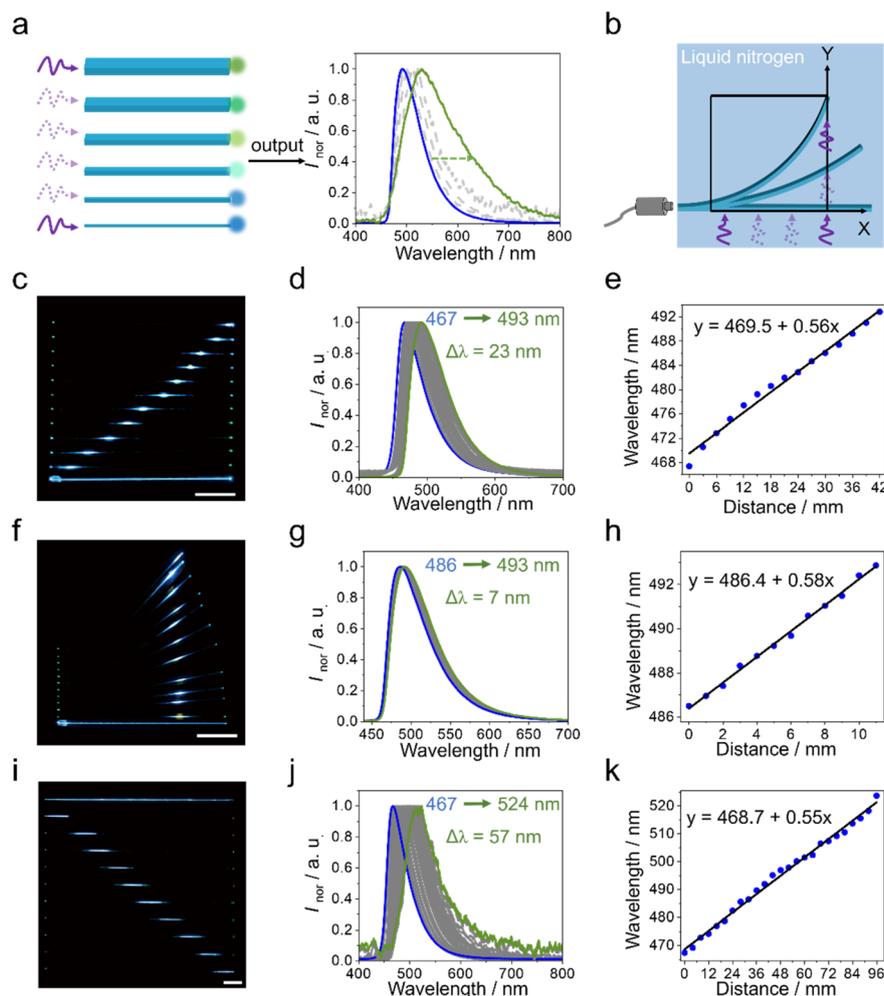

Fig. 5 (a) Diagram of different widths of crystal **1** applied as wavelength modulators. (b) Diagram of a spectral sensing system for real-time monitoring of two-dimensional motion in cryogenic environments. (c) Photograph of a crystal **1** excited by UV light in the *X* direction. (d) Normalized fluorescence spectra for acquisitions at different excitation positions. (e) Linear plot of the position shift *versus* spectral variation. (f) Photograph of crystal **1** excited by UV light in the *Y* direction. (g) Normalized fluorescence spectra for acquisitions at different depths. (h) Linear plot of depth position *versus* spectral variation. (i) Photographs of the decimeter-scale crystal **1** for optical signal transmission at the decimeter level. (j) Normalized fluorescence spectra for acquisitions at different excitation positions. (k) Linear plot of excitation position *versus* spectral variation. All the scales in the diagrams are 1 cm.

optical signal transmission capability of the machined crystals in both bent and straight states, at both room temperature and LN temperature.

Wavelength modulators are widely used in fields such as optical communications, laser technology and optical sensors.[11,29,52,56,57] As the width of crystal **1** affected the degree of red shifting of the wavelength during light transduction, the crystal was machined into structures of different widths. The outputs changed when the post-processed crystal was irradiated, indicating that wavelength modulators could be constructed (Fig. 5a). Thus, a spectral sensing system was designed to monitor the two-dimensional motion of an object in a cryogenic environment in real time (Fig. 5b) based on the redshift phenomenon in the emission spectrum of the optical signal from a crystal (Movie S4†). The crystal was placed on the surface of liquid nitrogen, and an optical signal receiver was installed at its left end. The crystal could be excited and its spectral signals collected by controlling the scanning of the UV light source along the *X* and *Y* axes. Along the *X*-axis, the UV light source was scanned horizontally to excite different positions of the crystal and generate corresponding spectral signals (Fig. 5b). The change pattern of these signals was analyzed in real time to accurately track the movement of the object along the *X*-axis. Similarly, the crystal was scanned along the *Y* using a vertically inserted UV light source (Fig. 5b), and the change in the position of the object along the *Y*-axis was detected by analyzing the spectral response at different depths. As a proof-of-concept, a crystal was placed on one side of a 3.2 cm × 3.2 cm rectangle, irradiated with UV light along the *X*-axis direction, and the spectral signals were collected at different positions (Fig. 5c). The spectral redshift reached a maximum of 23 nm, and the position of the shift showed a linear relationship with the wavelength (Fig. 5d and e). As shown in Fig. 5f, the spectral signals corresponding to different depths were collected by irradiating the crystal in *Y*-axis direction with a vertically inserted UV light source. The spectral redshift reached a maximum of 7 nm, and the depth showed a linear relationship with the spectrum (Fig. 5g and h). Furthermore, the decimeter-scale crystal exhibited excellent optical signal transmission along its entire length (Fig. 5i), and it showed a spectral redshift of up to 57 nm with the increase in distance between the UV excitation and the collected signal position (Fig. 5j). Meanwhile, the linear relationship between the excitation position and emission wavelength was still maintained (Fig. 5k). These unique optical properties indicate that the crystals can enable wide-range 2D object motion monitoring in cryogenic environments.

Conclusions

In summary, we have designed two organic crystals, **1** and **2**, derived from mono-benzene compounds. These crystals exhibited different growth lengths and mechanical properties. The crystallographic analysis revealed that noncovalent intermolecular interactions were the critical factors influencing different crystal growth behaviors and different mechanical properties at room and LN temperatures. The length of crystal **1**

exceeded 10 cm, which is the longest recorded in the field of elastic organic crystals. Furthermore, crystal **1** exhibited excellent flexibility and machinability at LN temperature as well as width-dependent optical waveguide outputs. These unique properties made it a promising material for the development of optical waveguide modulators and sensors that can be operated in extremely low temperatures, opening up new possibilities for real-time two-dimensional motion detection and precise optical signal modulation. This study not only advances the field of flexible organic crystals, but also expands applications of dynamic crystals for smart materials operated under extreme conditions.

Data availability

The data supporting this article have been included as part of the ESI.† Crystallographic data for the structures reported in this article have been deposited at the Cambridge Crystallographic Data Centre, under deposition numbers CCDC 2380818 (crystal **1**–298 K), CCDC 2380823 (crystal **1**–77 K), CCDC 2380824 (crystal **2**–298 K), and CCDC 2380828 (crystal **2**–77 K). These data can be obtained free of charge from The Cambridge Crystallographic Data Centre *via* **https://www.ccdc.cam.ac.uk/structures/**.

Author contributions

Tingting Ji performed the experiment and data analyses and wrote the manuscript draft. Xuesong Yang revised the manuscript. Quanliang Chen provided support for the single-crystal structural analysis. Hongyu Zhang conceived the ideas, designed the research, revised the manuscript and provided funding acquisition.

Conflicts of interest

There are no conflicts to declare.

Acknowledgements

Notes and references

1 W. M. Awad, D. W. Davies, D. Kitagawa, J. Mahmoud Halabi, M. B. Al-Handawi, I. Tahir, F. Tong, G. Campillo-Alvarado, A. G. Shtukenberg, T. Alkhidir, Y. Hagiwara, M. Almehairbi, L. Lan, S. Hasebe, D. P. Karothu, S. Mohamed, H. Koshima, S. Kobatake, Y. Diao, R. Chandrasekar, H. Zhang, C. C. Sun, C. Bardeen, R. O. Al-Kaysi, B. Kahr and P. Naumov, *Chem. Soc. Rev.*, 2023, **52**, 3098–3169.

2 S. Saha, M. K. Mishra, C. M. Reddy and G. R. Desiraju, *Acc. Chem. Res.*, 2018, **51**, 2957–2967.

3 A. Worthy, A. Grosjean, M. C. Pfrunder, Y. Xu, C. Yan, G. Edwards, J. K. Clegg and J. C. McMurtrie, *Nat. Chem.*, 2015, **7**, 65–72.

4 S. Bhunia, S. Chandel, S. K. Karan, S. Dey, A. Tiwari, S. Das, N. Kumar, R. Chowdhury, S. Mondal, I. Ghosh, A. Mondal, B. B. Khatua, N. Ghosh and C. M. Reddy, *Science*, 2021, **373**, 321–327.

5 Q. Di, M. B. Al-Handawi, L. Li, P. Naumov and H. Zhang, *Angew. Chem., Int. Ed.*, 2024, **63**, e202403914.

6 L. Li, J. Zhang, C. Yang, L. Huang, J. Zhang, J. Bai, C. Redshaw, X. Feng, C. Cao, N. Huo, J. Li and B. Z. Tang, *Small*, 2021, **17**, 2103125.

7 J. Gao, Y. Fan, Q. Zhang, L. Luo, X. Hu, Y. Li, J. Song, H. Jiang, X. Gao, L. Zheng, W. Zhao, Z. Wang, W. Ai, Y. Wei, Q. Lu, M. Xu, Y. Wang, W. Song, X. Wang and W. Huang, *Adv. Mater.*, 2022, **34**, 2107511.

8 Y. Qiu, H. Gao, S. Cao, Y. Zhang, Y. Wei, X. Wei, X. Li, X. Zhang, L. Jiang, Z. Zhao and Y. Wu, *Adv. Funct. Mater.*, 2024, **34**, 2313990.

9 C. Wei, L. Bai, X. An, M. Xu, W. Liu, W. Zhang, M. Singh, K. Shen, Y. Han, L. Sun, J. Lin, Q. Zhao, Y. Zhang, Y. Yang, M. Yu, Y. Li, N. Sun, Y. Han, L. Xie, C. Ou, B. Sun, X. Ding, C. Xu, Z. An, R. Chen, H. Ling, W. Li, J. Wang and W. Huang, *Chem*, 2022, **8**, 1427–1441.

10 K. Chen, J. Wang, W. Wu, H. Shan, H. Zhao, N. Wang, T. Wang, X. Huang and H. Hao, *Dyes Pigm.*, 2023, **219**, 111536.

11 S. Hayashi and T. Koizumi, *Angew. Chem., Int. Ed.*, 2016, **55**, 2701–2704.

12 S. Yousuf, J. Mahmoud Halabi, I. Tahir, E. Ahmed, R. Rezgui, L. Li, P. Laws, M. Daqaq and P. Naumov, *Angew. Chem., Int. Ed.*, 2023, **62**, e202217329.

13 H. Wang, Q. Tang, X. Zhao, Y. Tong and Y. Liu, *ACS Appl. Mater. Interfaces*, 2018, **10**, 2785–2792.

14 L. Li, P. Commins, M. B. Al-Handawi, D. P. Karothu, J. M. Halabi, S. Schramm, J. Weston, R. Rezgui and P. Naumov, *Chem. Sci.*, 2019, **10**, 7327–7332.

15 L. Lan, L. Li, Q. Di, X. Yang, X. Liu, P. Naumov and H. Zhang, *Adv. Mater.*, 2022, **34**, 2200471.

16 X. Yang, M. B. Al-Handawi, L. Li, P. Naumov and H. Zhang, *Chem. Sci.*, 2024, **15**, 2684–2696.

17 R. Chandrasekar, *Small*, 2021, **17**, 2100277.

18 S. Hayashi and T. Koizumi, *Chem.–Eur. J.*, 2018, **24**, 8507–8512.

19 S. Tang, K. Ye and H. Zhang, *Angew. Chem., Int. Ed.*, 2022, **61**, e202210128.

20 S. Tang, K. Ye, P. Commins, L. Li, P. Naumov and H. Zhang, *Adv. Opt. Mater.*, 2023, **11**, 2200627.

21 X. Pan, A. Zheng, X. Yu, Q. Di, L. Li, P. Duan, K. Ye, P. Naumov and H. Zhang, *Angew. Chem., Int. Ed.*, 2022, **61**, e202203938.

22 Z. Wang, W. Han, R. Shi, X. Han, Y. Zheng, J. Xu and X. Bu, *JACS Au*, 2024, **4**, 279–300.

23 R. P. Reed, R. E. Schramm and A. F. Clark, *Cryogenics*, 1973, **13**, 67–82.

24 Q. Ma, S. Liao, Y. Ma, Y. Chu and Y. Wang, *Adv. Mater.*, 2021, **33**, 2102096.

25 M. Okayasu and Y. Tsuchiya, *J. Sci.: Adv. Mater. Devices*, 2019, **4**, 577–583.

26 D. Ji, T. Jiang, Y. Zheng, Y. Sun, Z. Wei, L. Li and W. Hu, *Adv. Opt. Mater.*, 2022, **10**, 2102484.

27 J. Feng, J. Li and R. Liu, *Nano Energy*, 2024, **126**, 109651.

28 X. Yang, L. Lan, X. Pan, Q. Di, X. Liu, L. Li, P. Naumov and H. Zhang, *Nat. Commun.*, 2023, **14**, 2287.

29 L. Lan, L. Li, P. Naumov and H. Zhang, *Chem. Mat.*, 2023, **35**, 7363–7385.

30 J. Wu, S. Yao, H. Zhang, W. Man, Z. Bai, F. Zhang, X. Wang, D. Fang and Y. Zhang, *Adv. Mater.*, 2021, **33**, 2106175.

31 C. Jiang, Y. Shi, X. Yang, T. Zhao, J. Zhou, X. Jin, Y. Zhang and P. Duan, *Adv. Opt. Mater.*, 2023, **11**, 2300001.

32 Z. Xiang, Z. Wang, T. Ren, W. Xu, Y. Liu, X. Zhang, P. Wu, L. Yuan and X. Zhang, *Chem. Commun.*, 2019, **55**, 11462–11465.

33 J. Kim, J. H. Oh and D. Kim, *Org. Biomol. Chem.*, 2021, **19**, 933–946.

34 T. Raghava, A. Chattopadhyay, P. Bhavana and S. Banerjee, *Chem.–Asian J.*, 2023, **18**, e202201314.

35 T. Raghava, S. Banerjee and A. Chattopadhyay, *J. Org. Chem.*, 2023, **88**, 15708–15716.

36 T. Raghava, A. Chattopadhyay, S. Banerjee and N. Sarkar, *Org. Biomol. Chem.*, 2024, **22**, 364–373.

37 T. Raghava and S. Banerjee, *ChemistrySelect*, 2024, **9**, e202400831.

38 R. Huang, B. Tang, K. Ye, C. Wang and H. Zhang, *Adv. Opt. Mater.*, 2019, **7**, 1900927.

39 B. Tang, Z. Zhang, H. Liu and H. Zhang, *Chin. Chem. Lett.*, 2017, **28**, 2129–2132.

40 B. Tang, C. Wang, Y. Wang and H. Zhang, *Angew. Chem., Int. Ed.*, 2017, **56**, 12543–12547.

41 H. Liu, Z. Lu, Z. Zhang, Y. Wang and H. Zhang, *Angew. Chem., Int. Ed.*, 2018, **57**, 8448–8452.

42 H. Liu, Z. Bian, Q. Cheng, L. Lan, Y. Wang and H. Zhang, *Chem. Sci.*, 2019, **10**, 227–232.

43 P. R. Spackman, M. J. Turner, J. J. McKinnon, S. K. Wolff, D. J. Grimwood, D. Jayatilaka and M. A. Spackman, *J. Appl. Cryst.*, 2021, **54**, 1006.

44 M. J. Frisch, G. W. Trucks, H. B. Schlegel, G. E. Scuseria, M. A. Robb, J. R. Cheeseman, G. Scalmani, V. Barone, B. Mennucci, G. A. Petersson, H. Nakatsuji, M. Caricato, X. Li, H. P. Hratchian, A. F. Izmaylov, J. Bloino, G. Zheng, J. L. Sonnenberg, M. Hada, M. Ehara, K. Toyota, R. Fukuda, J. Hasegawa, M. Ishida, T. Nakajima, Y. Honda, O. Kitao, H. Nakai, T. Vreven, J. A. Montgomery Jr, J. E. Peralta, F. Ogliaro, M. Bearpark, J. J. Heyd, E. Brothers, K. N. Kudin, V. N. Staroverov, R. Kobayashi, J. Normand, K. Raghavachari, A. Rendell, J. C. Burant, S. S. Iyengar, J. Tomasi, M. Cossi, N. Rega, J. M. Millam, M. Klene, J. E. Knox, J. B. Cross, V. Bakken, C. Adamo, J. Jaramillo, R. Gomperts, R. E. Stratmann, O. Yazyev, A. J. Austin, R. Cammi, C. Pomelli, J. Ochterski, R. L. Martin, K. Morokuma, V. G. Zakrzewski, G. A. Voth, P. Salvador, J. J. Dannenberg, S. Dapprich, A. D. Daniels, O. Farkas, J. B. Foresman, J. V. Ortiz, J. Cioslowski and

D. J. Fox, *Gaussian 09, Revision D. 01*, Gaussian, Inc., Wallingford, CT, 2013.

45 S. Emamian, T. Lu, H. Kruse and H. Emamian, *J. Comput. Chem.*, 2019, **40**, 2868–2881.

46 Y. Ma, C. Xu, X. Mao, Y. Wu, J. Yang, L. Xu, M. Zhuo, H. Lin, S. Zhuo and X. Wang, *J. Am. Chem. Soc.*, 2023, **145**, 9285–9291.

47 V. V. Pradeep and R. Chandrasekar, *Adv. Opt. Mater.*, 2022, **10**, 2201150.

48 L. Lan, L. Li, X. Yang, P. Naumov and H. Zhang, *Adv. Funct. Mater.*, 2023, **33**, 2211760.

49 K. Zhao, T. F. Zhang, H. C. Chang, Y. Yang, P. S. Xiao, H. T. Zhang, C. X. Li, C. S. Tiwary, P. M. Ajayan and Y. S. Chen, *Sci. Adv.*, 2019, **5**, eaav2589.

50 Q. Chen, B. Tang, K. Ye and H. Zhang, *Adv. Mater.*, 2024, **36**, 2311762.

51 X. Pan, L. Lan, L. Li, P. Naumov and H. Zhang, *Angew. Chem., Int. Ed.*, 2024, **63**, e202320173.

52 Q. Di, L. Li, X. Miao, L. Lan, X. Yu, B. Liu, Y. Yi, P. Naumov and H. Zhang, *Nat. Commun.*, 2022, **13**, 5280.

53 Y. Li, Z. Ma, A. Li, W. Xu, Y. Wang, H. Jiang, K. Wang, Y. Zhao and X. Jia, *ACS Appl. Mater. Interfaces*, 2017, **9**, 8910–8918.

54 Y. Wei, X. Xu, X. Yang and H. Zhang, *Cryst. Growth Des.*, 2023, **23**, 8204–8211.

55 J. Qi, L. Lan, Q. Chen, L. Li, P. Naumov and H. Zhang, *Angew. Chem., Int. Ed.*, 2024, e202417409.

56 H. Wang, Y. Tong, X. Zhao, Q. Tang and Y. Liu, *Org. Electron.*, 2018, **61**, 304–311.

57 X. Ding, L. Wang, Y. Chang, C. Wei, J. Lin, M. Ding and W. Huang, *Aggregate*, 2024, **5**, e500.